



Three dimensional Z-scheme $(\text{BiO})_2\text{CO}_3/\text{MoS}_2$ with enhanced visible light photocatalytic NO removal

Ting Xiong^{a,1}, Mengqing Wen^{b,1}, Fan Dong^{a,*}, Jiayan Yu^c, Lulin Han^a, Ben Lei^a, Yuxin Zhang^d, Xiaosheng Tang^b, Zhigang Zang^{b,*}

^a Chongqing Key Laboratory of Catalysis and Functional Organic Molecules, College of Environment and Resources, Chongqing Technology and Business University, Chongqing 400067, China

^b Key Laboratory of Optoelectronic Technology and Systems of the Education Ministry of China, College of Optoelectronic Engineering, Chongqing University, Chongqing 400044, China

^c Chongqing Key Laboratory for Urban Atmospheric Environment Integrated Observation & Pollution Prevention and Control, Environmental Monitoring Center of Chongqing, Chongqing 401147, China

^d College of Materials Science and Engineering, National Key Laboratory of Fundamental Science of Micro/Nano-Devices and System Technology, Chongqing University, Chongqing 400044, China

ARTICLE INFO

Article history:

Received 9 February 2016

Received in revised form 4 June 2016

Accepted 10 June 2016

Available online 11 June 2016

Keywords:

Z-scheme photocatalysts

p-Type MoS_2

n-Type $(\text{BiO})_2\text{CO}_3$

NO removal

Visible light

ABSTRACT

The Z-scheme photocatalyst systems, with the redox ability of photogenerated electrons and holes unchanged and the efficient separate of carriers, have been under extensive investigation. Herein, we developed a facile method to prepare three dimensional Z-scheme $(\text{BiO})_2\text{CO}_3/\text{MoS}_2$ photocatalysts. Due to the enhanced visible light absorption, fast electrons and holes separate and transfer, the resulting three dimensional $(\text{BiO})_2\text{CO}_3/\text{MoS}_2$ photocatalysts exhibited high visible photocatalytic activity in the removal of NO in air, which exceeded those of the pristine $(\text{BiO})_2\text{CO}_3$ and MoS_2 . Electron spin resonance trapping results indicated that h^+ and $\cdot\text{O}_2^-$ were the main reactive species for NO removal. Although $(\text{BiO})_2\text{CO}_3$ is a n-type semiconductor while MoS_2 is a p-type semiconductor, a unique Z-scheme electron/hole transport mechanism instead of the p-n junction mechanism was proposed for the interfacial interaction between MoS_2 and $(\text{BiO})_2\text{CO}_3$ under visible light irradiation. The present work reveals a unique 3D Z-scheme photocatalyst system with p- and n-type semiconductors, and opens up new opportunities in designing hybrid photocatalysts with enhanced photocatalytic properties.

© 2016 Elsevier B.V. All rights reserved.

1. Introduction

The past decades have witnessed great advances concerning the synthesis, functionalization and application of three dimensional (3D) materials. 3D hierarchical materials have various attractive properties and widespread applications in catalysis, adsorption and separation, drug delivery and solar cells [1–6]. Recently, construction of 3D hierarchical structure becomes a hot research topic in photocatalysis [7–9].

As a typical Bi-based semiconductor, $(\text{BiO})_2\text{CO}_3$ has received increasing interest because of its promising applications in antibacterial, sensing, super capacitor and photocatalysis [10–13]. A variety of morphologies including hollow microspheres, rose-like and persimmon-like $(\text{BiO})_2\text{CO}_3$ have been successfully prepared

[14–16]. These $(\text{BiO})_2\text{CO}_3$ materials showed outstanding photocatalytic performance. However, the large band gap (ca. 3.4 eV) endows $(\text{BiO})_2\text{CO}_3$ with limited visible light activity. Thus, many strategies like metal deposition, nonmetal doping and semiconductor coupling have been applied to improve its visible light photocatalytic performance [17–21].

Generally, in contrast to a single component photocatalyst, hybrid photocatalysts present admirable properties [22–24]. For p–n junction photocatalysts, a built-in electrical potential is created between p- and n-type semiconductors when they are in contact. Driven by the electric field, the photogenerated electrons and holes are efficiently transferred and isolated, which inhibits their recombination [25–27]. However, the redox ability of photogenerated electrons and holes is weakened after charge carriers transfer. Recently, there is an increasing interest in the design and fabrication of Z-scheme photocatalysts to achieve enhanced photocatalytic performance. This mechanism makes a composite photocatalyst utilize both reduction ability for one semiconductor

* Corresponding authors.

E-mail addresses: dfctbu@126.com (F. Dong), zangzg@cqu.edu.cn (Z. Zang).

¹ These authors contributed equally to this work.

with more negative conduction band potential and oxidation abilities of another semiconductor with more positive valence band potential [28–34]. Thus, Z-scheme photocatalytic systems are more desirable than p–n junction systems in preserving the original redox ability.

(BiO)₂CO₃, as a typical p-type semiconductor, has been selected to couple with n-type semiconductors. Cao' group prepared p–n junction photocatalysts BiOI/(BiO)₂CO₃ with higher photocatalytic activity than pure (BiO)₂CO₃ and BiOI for the degradation of methyl orange [35]. Qian et al. synthesized Ag₂O/Bi₂O₂CO₃ p–n heterojunctions with enhanced photocatalytic activity toward the removal of Rhodamine B, methyl blue and methyl orange [36]. To date, no researches has been reported to enhance the photocatalytic performance of (BiO)₂CO₃ via constructing Z-scheme photocatalytic systems. MoS₂, a transitional metal dichalcogenides semiconductor with an indirect band gap of about 1.3 eV, exhibits p-type properties and has been used for modifying other semiconductor photocatalysts [37–41]. The TiO₂@MoS₂ heterostructure achieved high photocatalytic hydrogen production, which resulted from the positive synergetic effect between the MoS₂ and TiO₂ [42]. Improvement in UV light photocatalytic activity has been observed for MoS₂/Bi₂O₂CO₃ composites as well, but no research about the enhanced visible photocatalytic activity for MoS₂/Bi₂O₂CO₃ is studied [43]. Yet, the photocatalysis mechanism is not clear. These scientific problems push us to design novel (BiO)₂CO₃/MoS₂ photocatalysts for enhanced visible light activity and focus on the actual photocatalytic mechanism of the (BiO)₂CO₃/MoS₂ composites.

In this work, 3D (BiO)₂CO₃/MoS₂ composites photocatalysts were prepared by a simple method. Despite MoS₂ and Bi₂O₂CO₃ are p-type and n-type semiconductor, respectively, the p–n junction photocatalytic mechanism between MoS₂ and Bi₂O₂CO₃ wasn't observed. Instead, a novel Z-scheme electron/hole transport mechanism was observed. The excellent photocatalytic activities of the as-prepared (BiO)₂CO₃/MoS₂ were assessed by removal of NO in air under visible light irradiation. The high photocatalytic performance was benefited from the improved visible light absorption and efficient separation of photo-induced electron–hole pairs. Moreover, the 3D hierarchical structures contributed to the visible light absorption and diffusion of products. The •O²⁻ and h⁺ radicals were found to be the main reactive species accounting for NO removal. This work provides a new understanding of the Z-scheme photocatalysts composing of p- and n-type semiconductors, thus offering new insights into the design of hybrid photocatalysts with high performance.

2. Experimental

2.1. Materials and synthesis

All chemicals used in this study were analytical grade (Sigma Aldrich) and were used without further purification. In a typical synthesis, MoS₂ was synthesized using a hydrothermal method [44]. Typically, Na₂MoO₄ (250 mg) and thioacetamide (200 mg) were dissolved in 60 mL of deionized H₂O. The mixture was then transferred to a 100 mL Teflon-lined autoclave and kept at 200 °C for 16 h. After cooling down, the precipitates were collected and washed with water and ethanol for three times.

The (BiO)₂CO₃/MoS₂ composites were prepared by a simple hydrothermal method. A appropriate amount of MoS₂ was added into 70 mL of water and ultrasound for 30 min. Then, sodium carbonate (0.46 g) was added into the above suspension and stirred for 10 min. Next, bismuth citrate (1.60 g) was added into the above mixed solution and stirred for 30 min. The resulting suspension was then hydrothermally treated at 160 °C for 24 h. After the reaction, the sample obtained was filtered, washed with water and ethanol

for three times and dried at 70 °C for 12 h to get final products without further treatment. According to the molar ratio of MoS₂ to (BiO)₂CO₃ is 1%, 5% and 10%, the obtained sample was denoted as BOC-MoS₂-1%, BOC-MoS₂-5% and BOC-MoS₂-10%, respectively. The sample without adding MoS₂ was labeled as BOC.

2.2. Characterization

The crystal phases of the samples were analyzed by X-ray diffraction (XRD) with Cu Kα radiation (model D/max RA, Rigaku Co., Japan). Scanning electron microscopy (SEM; model JSM-6490, JEOL, Japan) and Transmission electron microscopy (TEM; JEM-2010, Japan) were used to characterize the morphology of the obtained products. X-ray photoelectron spectroscopy (XPS) with Al Kα X-rays radiation operated at 150 W (Thermo ESCALAB 250, USA) was used to investigate the surface properties. The UV–vis diffuse-reflectance spectrometry (DRS) spectra were obtained for the dry-pressed disk samples using a Scan UV–vis spectrophotometer (UV–vis DRS, UV-2450, Japan) equipped with an integrating sphere assembly, using 100% BaSO₄ as the reflectance sample. Nitrogen adsorption–desorption isotherms were obtained on a nitrogen adsorption apparatus (ASAP 2020, USA). All the samples were degassed at 120 °C prior to measurements. The samples for electron spin resonance (ESR) measurement were prepared by mixing the as-prepared samples in a 50 mM DMPO solution tank (aqueous dispersion for DMPO•OH and methanol dispersion for DMPO•O₂⁻, 420 nm visible light irradiation). The electrochemical impedance spectra (ESI) measurements were performed in three-electrode quartz cells with a 0.1 M Na₂SO₄ electrolyte solution. Platinum wire was used as the counter electrode, and saturated calomel electrodes were used as the reference electrodes. (BiO)₂CO₃ and (BiO)₂CO₃/MoS₂ film electrodes on ITO served as the working electrode. The photoelectrochemical experiment results were recorded using an electrochemical system (CHI-660B, China). All the photoelectrochemical measurements were performed under visible light of a 500 W Xe lamp coupling with 420 nm cutoff filters, and the average light power was 45 mW/cm².

2.3. Evaluation of photocatalytic activity

The as-prepared samples were applied for photocatalytic removal of NO at ppb level in a continuous flow reactor under visible light irradiation. The reactor was 4.5 L (30 cm × 15 cm × 10 cm), made of polymeric glass, and covered with Saint-Glass. A commercial tungsten halogen lamp (150 W) was vertically placed 20 cm above the reactor. A UV cut-off filter (420 nm) was applied to remove UV light for the test of photocatalytic activity in visible light region (420–780 nm), and the average light intensity was 0.16 W cm⁻². The as-prepared sample (0.20 g) was dispersed in distilled water (50 mL) in a beaker via ultrasonic treatment for 10 min and then coated onto two glass dishes (12.0 cm in diameter). The coated dishes were pretreated at 70 °C to remove water in the suspension and were placed at the center of the reactor. The NO gas was acquired from a compressed gas cylinder at a concentration of 100 ppm of NO (N₂ balance). The initial concentration of NO was diluted to about 600 ppb. The flow rates of the air stream and NO were controlled at 2.4 L/min and 15 mL/min, respectively. The two gas streams were then premixed in a three-way valve. The relative humidity is controlled at 50% in the air stream. When the adsorption–desorption equilibrium was achieved, the lamp was turned on. The concentration of NO was measured every one min by using a NOx analyzer (Thermo Scientific, 42i-TL), which also monitored the concentration of NO₂ and NOx (NOx represents NO + NO₂). The removal ratio (η) of NO was calculated using η (%) = (1 – C/C₀) × 100%, where C is the outlet concentration of NO

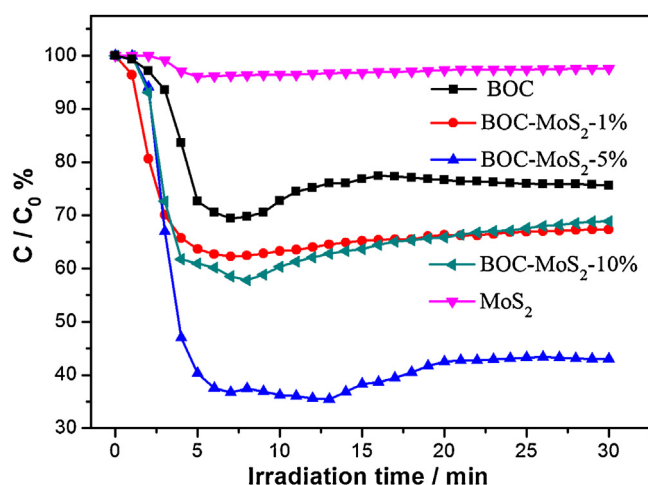


Fig. 1. Photocatalytic activity of the as-prepared $(\text{BiO})_2\text{CO}_3$, MoS_2 and $(\text{BiO})_2\text{CO}_3/\text{MoS}_2$ composites towards the removal of NO under visible light irradiation.

after reaction for time t , and C_0 represent the inlet concentration after achieving adsorption-desorption equilibrium.

3. Results and discussion

3.1. Photocatalytic activity for NO removal

Photocatalytic removal of NO under visible light irradiation was employed as a model reaction to probe the photocatalytic performance of the as-prepared photocatalyst. As shown in Fig. 1, after irradiation for 30 min, the bare $(\text{BiO})_2\text{CO}_3$ presents certain activity (24% of NO removal ratio). Based on our previous research, the as-prepared $(\text{BiO})_2\text{CO}_3$ contains some intrinsic defects. When incident light is irradiated in these sites, holes and electrons can be produced. As the as-prepared $(\text{BiO})_2\text{CO}_3$ are three dimensional microspheres structures, light absorption can be increased via reflecting and scattering effects. Thus, this photocatalytic activity for $(\text{BiO})_2\text{CO}_3$ is due to the increased extrinsic absorption originating from the strong reflecting and scattering effects of incident light in 3D structure [20,45]. The bare MoS_2 with a small band gap shows negligible photoactivity mainly because of the fast recombination of carriers. When combining $(\text{BiO})_2\text{CO}_3$ with MoS_2 , the enhanced activity is obtained. The photocatalytic activities of $(\text{BiO})_2\text{CO}_3/\text{MoS}_2$ photocatalysts increase gradually at first and then decrease with an increasing proportion of MoS_2 . NO removal ratio over BOC-MoS₂-1% reaches 33%. In particular, BOC-MoS₂-5% exhibits the highest photocatalytic activity with a NO removal ratio of 57%.

This high photocatalytic performance may be benefited from the enhanced light absorption, efficient charge transfer and intimate contact between $(\text{BiO})_2\text{CO}_3$ and MoS_2 . The detailed mechanism will be discussed later. BOC-MoS₂-10% displays inferior photocatalytic performance, but it is still higher than those of BOC and bare MoS_2 . The decrease in activity of the samples with a heavy loading of MoS_2 may block the absorption of the incident light. Similar case has been observed for $\text{MoS}_2/\text{mpg-CN}$ photocatalysts [46].

3.2. Phase and composition

The purity and crystalline phase of the as-obtained samples were characterized by XRD patterns as depicted in Fig. 2a. The peaks observed with BOC can be assigned to the characteristic peaks of standard card of $(\text{BiO})_2\text{CO}_3$ (JCPDS-ICDD card no. 25-1464), indicating the purity of the as-obtained BOC. For MoS_2 , all the diffraction peaks can be indexed to the hexagonal phase of MoS_2 (JCPDS:65-1951), and the weak peaks imply the poor crystallinity. The major diffraction peaks at $2\theta = 13.8^\circ$, 33.1° and 58.5° can be well attributed to the (002), (100) and (110) planes of MoS_2 . However, no XRD peaks of MoS_2 are found for BOC-MoS₂-1% due to the low content of MoS_2 . A weak peak at $2\theta = 13.8^\circ$ belonging to MoS_2 is observed in BOC-MoS₂-5% and BOC-MoS₂-10%. Besides, from the enlarged view (Fig. 2b), there are obvious changes of intensities, widths and positions. Compared with BOC, the peaks of $(\text{BiO})_2\text{CO}_3$ in the as-prepared $(\text{BiO})_2\text{CO}_3/\text{MoS}_2$ composites are weakened and widened, which suggest that the introduction of MoS_2 affects the crystallinity and growth of $(\text{BiO})_2\text{CO}_3$. The peak at $2\theta = 32.7^\circ$ experiences chemical shift, revealing the intimate contact and strong interaction between MoS_2 and $(\text{BiO})_2\text{CO}_3$.

To further probe the chemical nature of the $(\text{BiO})_2\text{CO}_3/\text{MoS}_2$ composites, X-ray photoemission spectroscopy was performed as shown in Fig. 3. For BOC-MoS₂-10%, two peaks of Bi 4f in Fig. 3a at 164.4 and 159.1 eV are assigned to Bi 4f_{5/2} and Bi 4f_{7/2}, respectively [15]. The binding energies of C 1s at 284.7, 286 and 287.8 eV are originated from the adventitious carbon species from XPS measurement, and the binding energy located at 288.7 eV corresponds to carbonate ion in $(\text{BiO})_2\text{CO}_3$ (Fig. 3b). As shown in Fig. 3c, three peaks at 530, 531 and 532.5 eV are observed for O 1s. The peak at 530 eV is associated with Bi-O binding energy in $(\text{BiO})_2\text{CO}_3$, and the peaks at around 531 and 532.5 eV attribute to carbonate species and adsorbed H₂O on the surface [15]. For MoS_2 (Fig. 3d), it can be clearly seen that the peaks at ca. 231.9 and 228.7 eV are ascribed to the Mo 3d_{3/2} and Mo 3d_{5/2} of Mo⁴⁺, respectively [46]. The peak with binding energy at about 225.8 eV is for the S 2s, corresponding to the characteristics of S²⁻. Notably, besides the XPS peaks about Mo⁴⁺ and S²⁻, weak peaks for Mo 3d at 232.4 and 235.2 eV are also observed in the BOC-MoS₂-10% composite, implying the existence

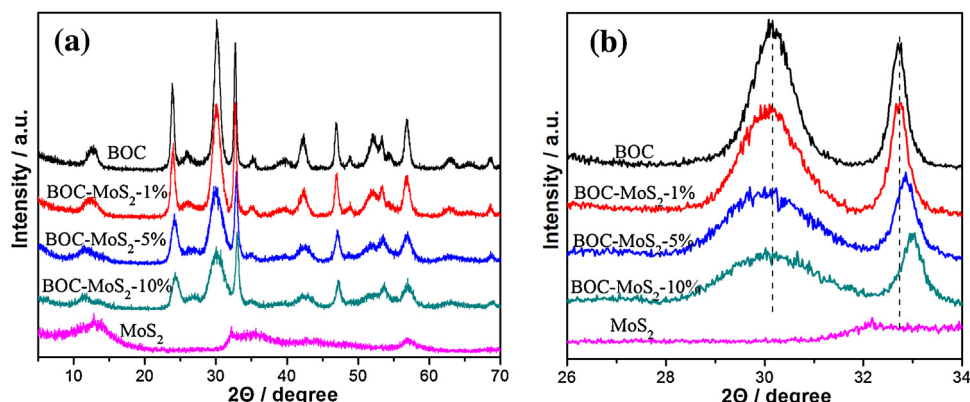


Fig. 2. XRD (a) and the enlarged view of $2\theta = 26\text{--}34^\circ$ diffraction region (b) of the synthesized five samples.

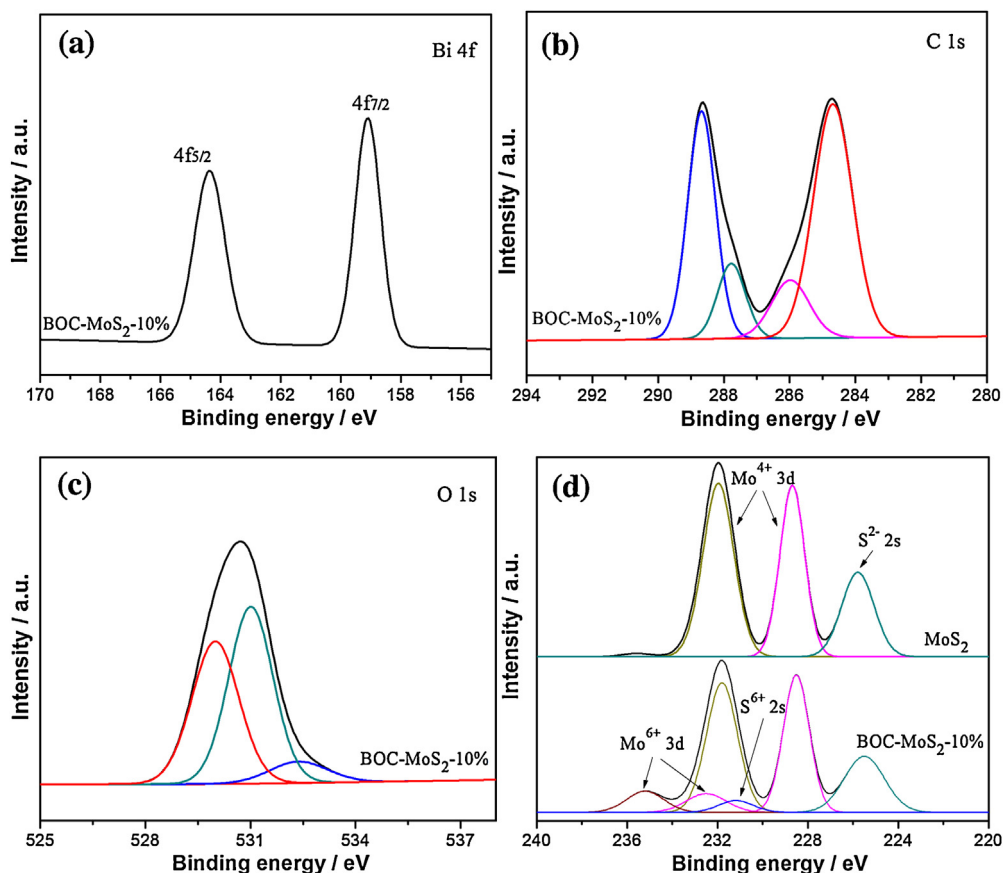


Fig. 3. XPS spectra of the as-prepared MoS₂ and BOC-MoS₂-10% samples, Bi 4f (a), C 1s (b), O 1s (c), Mo 3d and S 2s (d).

of Mo⁶⁺ state, presumably due to the formation of small amounts of surface oxide species during the hydrothermal reaction [46]. The XPS peaks of Mo and S elements experience chemical shifts in the composite relative to those of pure MoS₂, indicating the presence of strong interactions between MoS₂ and (BiO)₂CO₃. These results confirm the existence of MoS₂ and the successful fabrication of (BiO)₂CO₃/MoS₂ composites.

3.3. Morphology

The morphology and microstructures of the as-prepared samples were characterized by SEM and TEM. The SEM image of pristine MoS₂ (Fig. 4a) shows microflower morphology. A magnified SEM image in Fig. 4b shows that the microflowers are loosely composed of randomly oriented nanosheets with a thickness of around 40 nm. However, for BOC-MoS₂-5%, well-defined (BiO)₂CO₃ hierarchical microspheres with the diameter of 1–1.5 μm can be observed. And MoS₂ microflowers exist in the voids between the (BiO)₂CO₃ microspheres, which act as a bridge among these (BiO)₂CO₃ microspheres (Fig. 4c and d). Notably, many pores are generated in these microflowers and microspheres, which can improve the utilization of incident light and serve as transport paths for molecules [1]. TEM images of the BOC-MoS₂-5% sample are presented in Fig. 4e and f. It shows that intimate contact exists between MoS₂ and (BiO)₂CO₃. A fringe with lattice spacing of approximately 0.62 nm is observed in the HRTEM image (Fig. 4e), corresponding to the (002) plane of hexagonal MoS₂. Also, the well-defined crystalline structures of (BiO)₂CO₃ are illustrated by the lattice fringes with a lattice spacing of 0.34 nm, corresponding to the plane of (004) (Fig. 4f). As can be seen, 3D (BiO)₂CO₃/MoS₂ composites with close contact have been successfully fabricated.

3.4. Pores structures

The adsorption capacity of materials is related to its S_{BET} , and the higher adsorption capacity allows the materials to adsorb more reactant for the photocatalytic reactions. The BET surface areas of MoS₂, BOC-MoS₂-1%, BOC-MoS₂-5% and BOC-MoS₂-10% are 40.6, 50, 44.5, 42.2 m²/g, respectively, which are close to that of BOC (40 m²/g), demonstrating that the introduction of MoS₂ has little effect on the surface area. The N₂ adsorption–desorption isotherm of the five samples can be ascribed to a type-IV isotherm (Fig. 5a), suggesting the presence of mesopores [47]. The pore size distribution curves are quite broad as shown in Fig. 5b. BOC and the composites show small mesopores at ca. 3.8 nm. All the samples exhibit mesopores and macropores from 10 to 100 nm. These pores are formed by the aggregated nanosheets. Though their BET surface areas are not large, such hierarchical structures with mesopores and macropores can function as efficient transport paths for reactants and products in photocatalytic reactions [1,45].

3.5. Light absorption and carriers transfer

The light absorption property of the samples is demonstrated by UV–vis DRS spectra and displayed in Fig. 6a. Pure (BiO)₂CO₃ sample exhibits its fundamental absorption sharp edge rising at 380 nm, suggesting that BOC is only UV response. MoS₂ almost shows complete absorption in the UV and visible light region for its narrow band gap. Importantly, the (BiO)₂CO₃/MoS₂ composites exhibit boosted visible light absorption. Upon increasing the MoS₂ loading amount, the absorption intensity of the composites in the visible range increases gradually relative to the bare (BiO)₂CO₃. These are induced by the strong optical absorption of

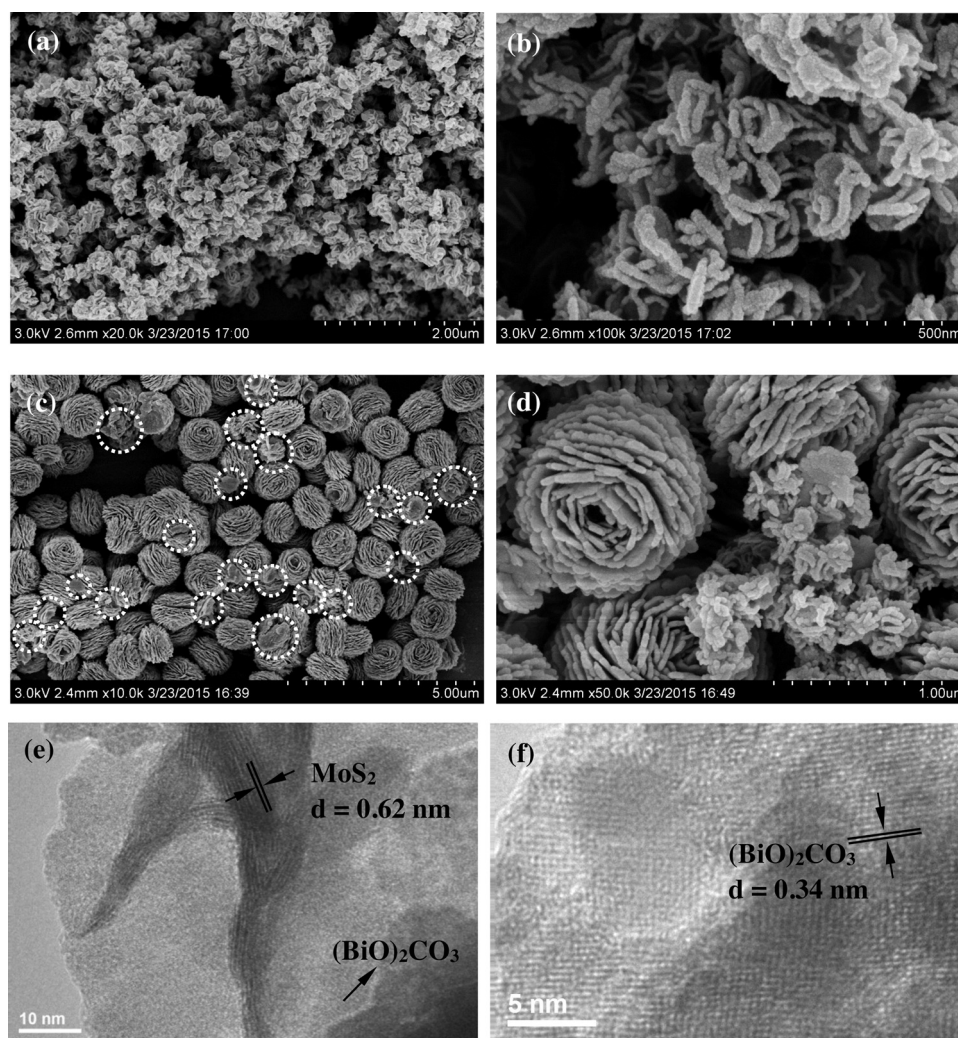


Fig. 4. SEM of MoS₂ (a,b) and BOC-MoS₂-5% (c,d), and TEM of BOC-MoS₂-5% (e,f).

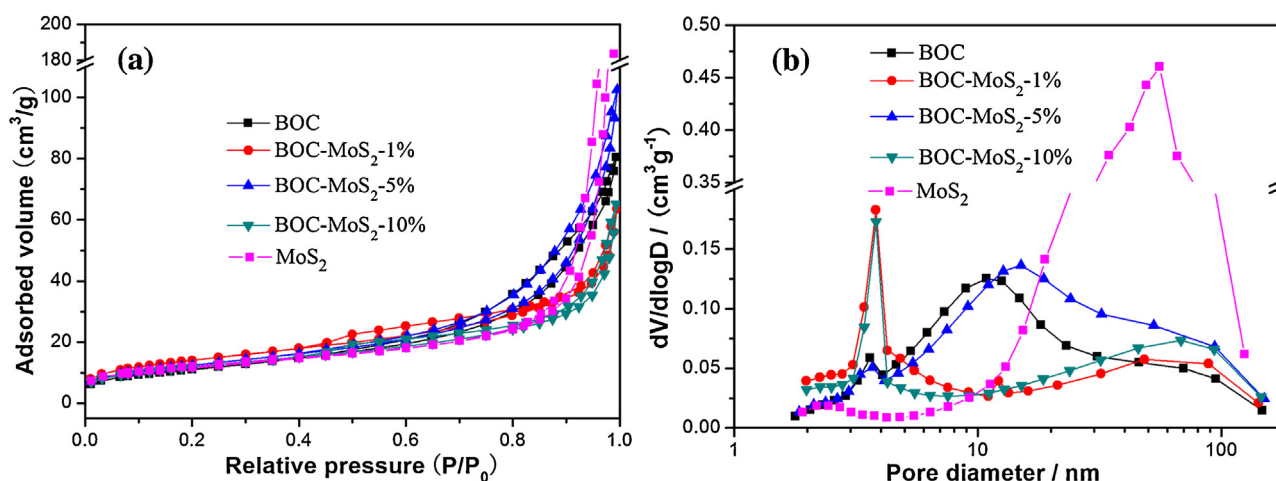


Fig. 5. BET adsorption-desorption isotherms (a) and the corresponding pore size distribution (b) of the as-prepared samples.

black MoS₂ and the strong interactions between (BiO)₂CO₃ and MoS₂ on the interface. To get deeper insights into the separation of photo-generated carriers, the electrochemical impedance spectra (EIS) of (BiO)₂CO₃ and the composites were explored. As shown in Fig. 6b, the Nyquist radii of the (BiO)₂CO₃/MoS₂ composites are

smaller than that of (BiO)₂CO₃ under visible light irradiation. It is reported that the smaller arc in an EIS Nyquist plot implies a smaller charge-transfer resistance on the electrode surface [48]. Thus, the addition of MoS₂ could efficiently promote the migration of photo-generated holes and electrons. BOC-MoS₂-5% shows the smallest

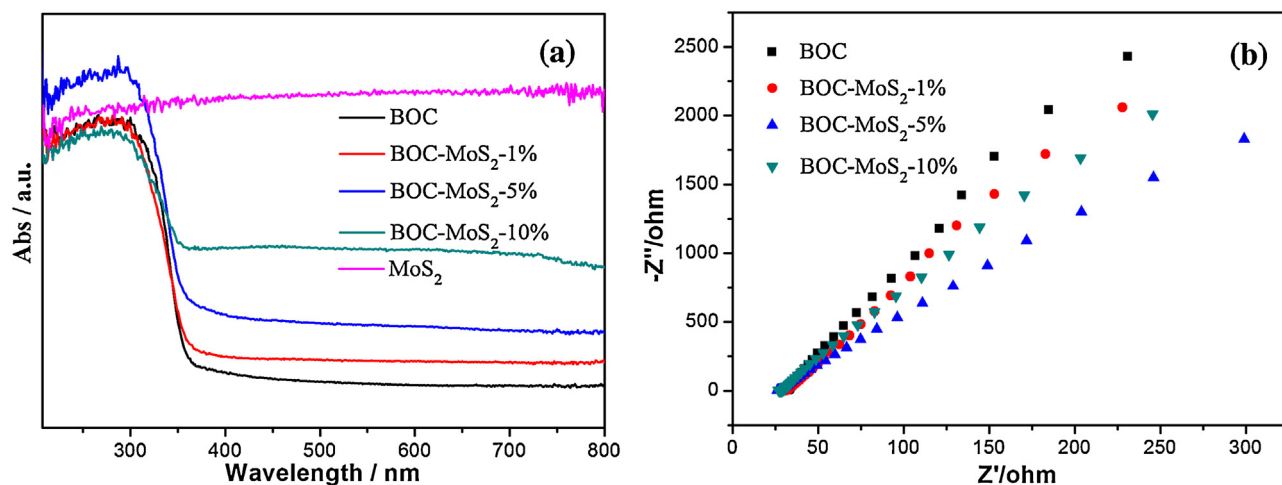


Fig. 6. UV-vis DRS spectra (a) and the electrochemical impedance spectra (b) of the as-obtained samples.

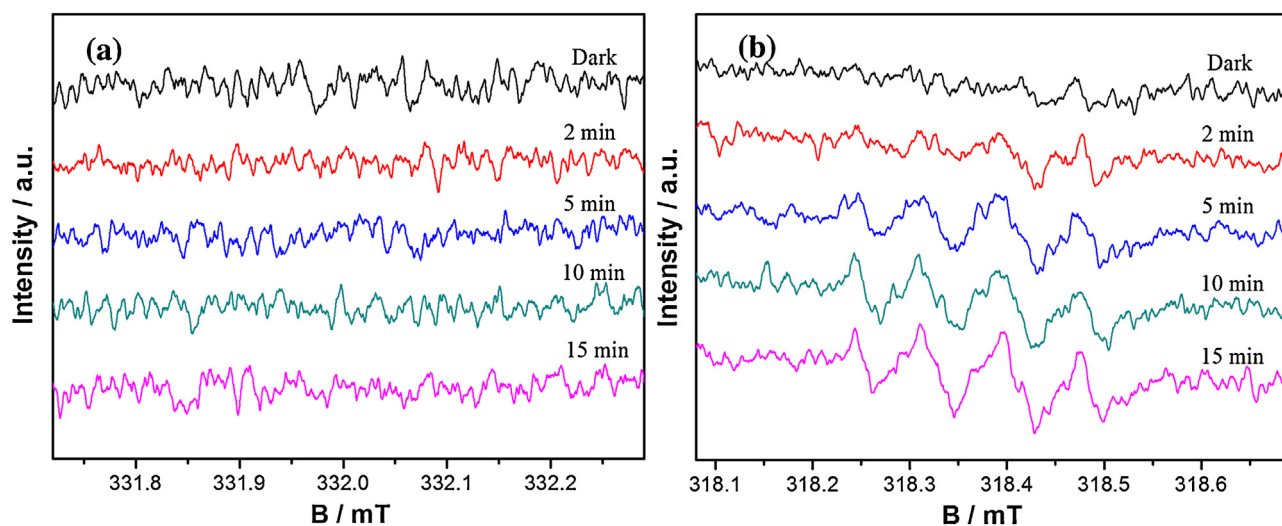


Fig. 7. DMPO spin-trapping ESR spectra of BOC-MoS₂-5% in an aqueous dispersion for DMPO·OH (a) and in a methanol dispersion for DMPO·O₂⁻ (b).

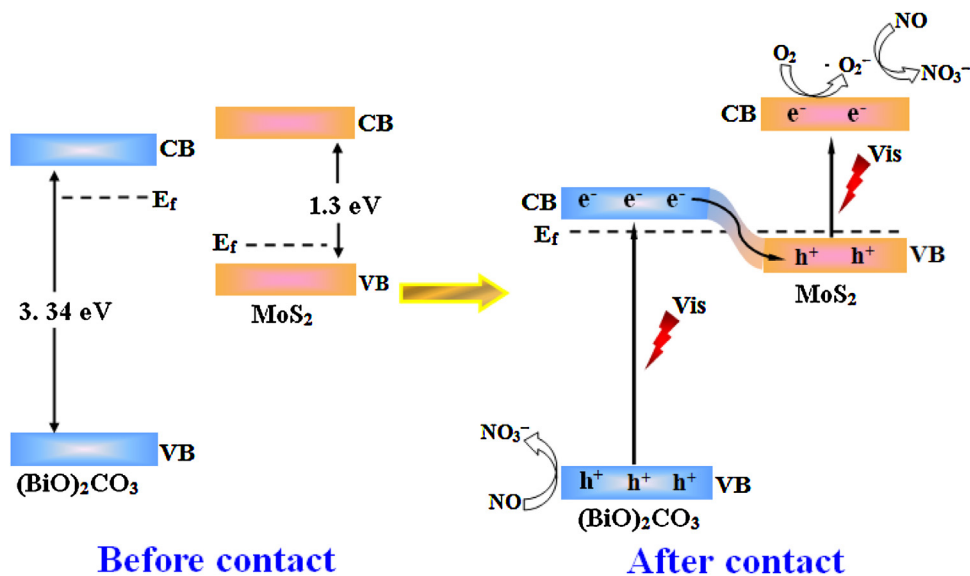


Fig. 8. The proposed photocatalytic mechanism of the as-prepared samples.

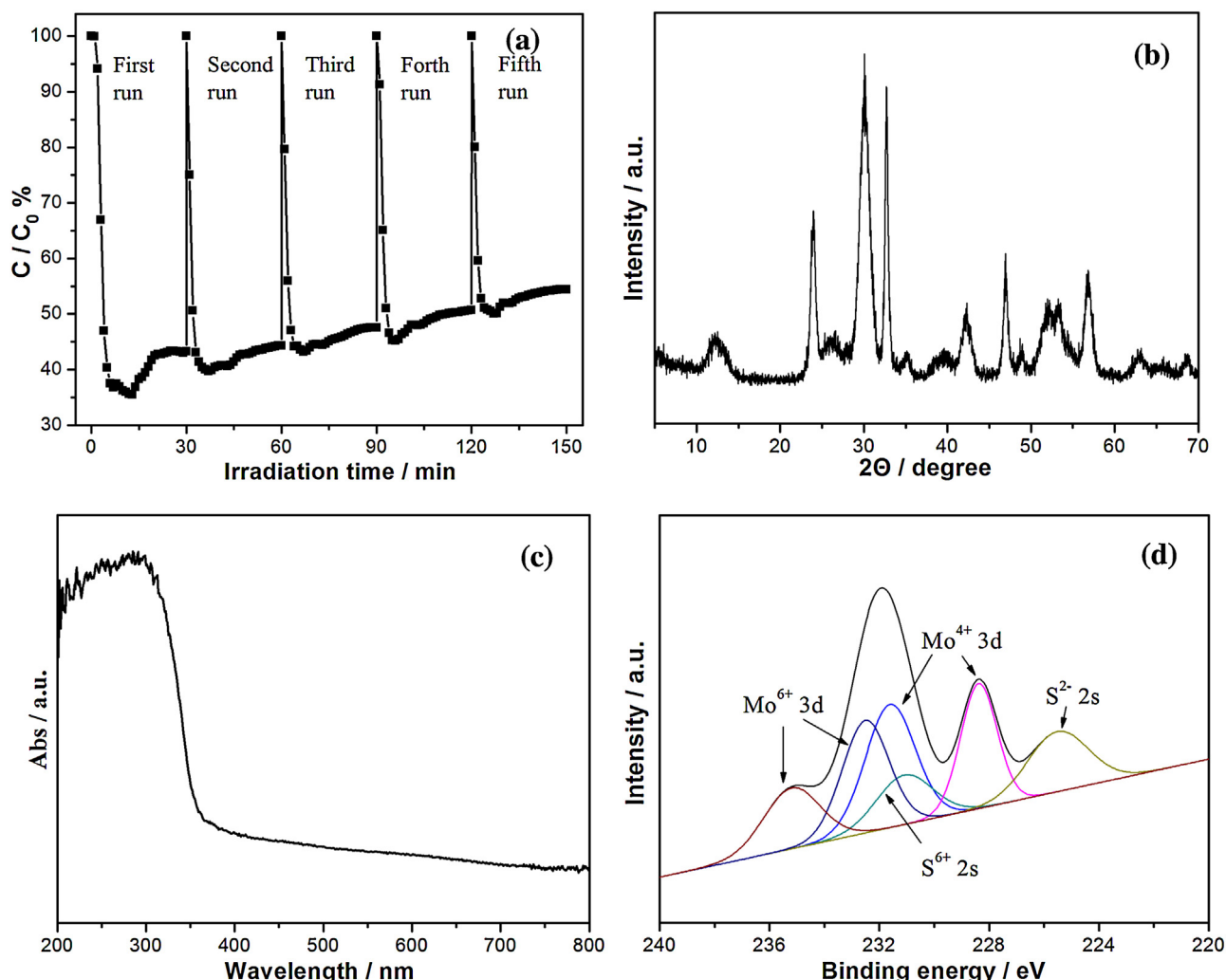


Fig. 9. Cycle photocatalytic performance of BOC-MoS₂-5% (a), XRD (b), UV-vis DRS spectra (c) and XPS (d) of the BOC-MoS₂-5% sample after cycle tests.

Nyquist radii, which is expected to possess the best separate ability of charge carriers among the as-prepared samples.

3.6. Photocatalytic mechanism for NO removal

It is well-known that the photocatalytic process is induced by photogenerated electron–hole pairs. These active holes and electrons then react with O₂/H₂O/OH[−] to yield other active species [49]. ESR spin-trap with DMPO technique has been carried out to identify the main active species. In the dark, no signals can be detected. Under visible light irradiation, surprisingly, no characteristic peaks about DMPO-•OH is observed when detecting the •OH production by ESR (Fig. 7a). (BiO)₂CO₃ can be excited to create holes and electrons under visible light irradiation, and holes then induce the production of •OH based on our previous report [45]. Herein, no signals about •OH are detected probably because the holes directly react with reactants instead of oxidizing H₂O/OH[−] to produce •OH. However, four characteristic peaks of the DMPO-•O₂[−] are found, and their intensity increases with the irradiation time (Fig. 7b), confirming the generation of •O₂[−]. In the present system, holes and •O₂[−] are regarded as the main active species during the photocatalytic NO removal processes with the illuminated BOC-MoS₂-5% photocatalyst.

Based on the above-mentioned analysis, we propose the photocatalytic mechanism as illustrated in Fig. 8. The relative conduction band and valence band positions of single (BiO)₂CO₃ and MoS₂ are

shown in the left of Fig. 8 [50,51]. When intimate contact between them are formed, the conduction band and valence band positions of (BiO)₂CO₃ and MoS₂ change to reach equilibration of Fermi levels (E_f). Finally, the energy bands of (BiO)₂CO₃ shift downward along with the E_f , whereas those of MoS₂ shift upward in this process. The newly formed energy band structures become to the interactive structure (the right of Fig. 8) [35,36]. Under visible light irradiation, (BiO)₂CO₃ and MoS₂ could be double-excited and electron–hole pairs would be generated. (BiO)₂CO₃ is a n-type semiconductor and MoS₂ is a p-type semiconductor. But here, the *p-n* junction mechanism isn't proposed to occur because the electrons on the conduction band of (BiO)₂CO₃ are not strong enough to induce the creation of •O₂[−] and the holes in the valence band of MoS₂ cannot directly oxidize NO. Instead, the electrons are excited to the conduction band of (BiO)₂CO₃ from its valence band, then they transfer and recombine with the photogenerated holes in the valence band of MoS₂. As such, the holes left in the valence band of (BiO)₂CO₃ can directly oxidize the surrounding NO to harmless products like NO₃[−]. Simultaneously, the up-shift of conduction band of MoS₂ leads to more powerful electrons, which could be trapped by O₂ in air near the surface to yield •O₂[−], which subsequently participate in the removal of NO.

As a result, the photoinduced electrons and holes are spatially isolated, which greatly retard their undesirable recombination. Importantly, the redox ability of photogenerated electrons and holes isn't weakened after charge transfer. Obviously, a unique Z-

scheme electron/hole transport mechanism is observed. Besides, the pores in 3D hierarchical structure could serve as transport paths for reactants and products and increase the absorption of incident light. Therefore, $(\text{BiO})_2\text{CO}_3/\text{MoS}_2$ photocatalysts exhibit high photocatalytic properties on the removal of NO under visible-light irradiation.

3.7. Stability and deactivation mechanism

The stability of the composites photocatalyst was evaluated by repeating experiments on the removal of NO under visible irradiation using BOC- MoS_2 -5%. As shown in Fig. 9a, the photocatalytic efficiency shows loss after five successive cycles, indicating that photocatalyst becomes deactivated. To reveal the reason for this deactivation, we tested the XRD spectra, UV–vis DRS spectra and XPS spectra of the used BOC- MoS_2 -5% sample. Compared with the fresh BOC- MoS_2 -5%, the XRD spectrum (Fig. 9b) and UV–vis DRS spectrum (Fig. 9c) of the used sample don't show obvious change. Notably, the XPS analysis in Fig. 9d shows that the peaks intensity of Mo^{6+} and S^{6+} increase while Mo^{4+} and S^{2-} decrease. Namely, the oxidation/corrosion of MoS_2 by photogenerated holes occurs over the BOC- MoS_2 -5% photocatalysts, accounting for its deactivation during the prolonged operations. This phenomenon has been observed in $\text{MoS}_2/\text{g-C}_3\text{N}_4$ photocatalysts as well [46]. The stability of $(\text{BiO})_2\text{CO}_3/\text{MoS}_2$ composites can be improved by introducing graphene, and this separate work will be reported in the future.

4. Conclusions

In summary, 3D Z-scheme $(\text{BiO})_2\text{CO}_3/\text{MoS}_2$ photocatalysts were successfully synthesized by a facile method. The resulted 3D $(\text{BiO})_2\text{CO}_3/\text{MoS}_2$ photocatalysts exhibited high visible photocatalytic activity in removing NO superior to those of bare $(\text{BiO})_2\text{CO}_3$ and MoS_2 . The enhanced photocatalytic activity could be ascribed to the formation of Z-scheme $(\text{BiO})_2\text{CO}_3/\text{MoS}_2$ structure and the 3D hierarchical structure. The unique Z-scheme electron/hole transport mechanism efficiently separated the photoinduced carriers and didn't weaken the redox ability of photogenerated electrons and holes. The pores in 3D hierarchical structure acted as transport paths for molecules and increased the absorption of incident light. Active species like h^+ and $\cdot\text{O}_2^-$ were proposed to be responsible for NO removal over $(\text{BiO})_2\text{CO}_3/\text{MoS}_2$ photocatalyst. The deactivation mechanism of the $(\text{BiO})_2\text{CO}_3/\text{MoS}_2$ during repeated irradiation was revealed, which was associated with the oxidation/corrosion of MoS_2 . This finding provides unprecedented insights on Z-scheme photocatalysts associated with p- and n-type semiconductor, and opens up an appealing strategy for the development of composites photocatalysts with high performance.

Acknowledgments

This research is financially supported by the National Natural Science Foundation of China (51478070, 51108487, 61520106012, 61574024), and the innnovation project from CTBU (153005).

References

- [1] C.M.A. Parlett, K. Wilson, A.F. Lee, Hierarchical porous materials: catalytic applications, *Chem. Soc. Rev.* 42 (2013) 3876–3893.
- [2] H. Wang, A.L. Rogach, Hierarchical SnO_2 nanostructures: recent advances in design, synthesis, and applications, *Chem. Mater.* 26 (2014) 123–133.
- [3] Y. Li, J. Shi, Hollow-structured mesoporous materials: chemical synthesis, functionalization and applications, *Adv. Mater.* 26 (2014) 3176–3205.
- [4] D. Fattakhova-Rohlfing, A. Zaleska, T. Bein, Three-dimensional titanium dioxide nanomaterials, *Chem. Rev.* 114 (2014) 9487–9558.
- [5] K.C. Hribar, P. Soman, J. Warner, P. Chung, S. Chen, Light-assisted direct-write of 3D functional biomaterials, *Lab Chip* 14 (2014) 268–275.
- [6] A. Di Paola, E. García-López, G. Marci, L. Palmisano, A survey of photocatalytic materials for environmental remediation, *J. Hazard. Mater.* 211–212 (2012) 3–29.
- [7] C.T. Dinh, H. Yen, F. Kleitz, T.O. Do, Three-dimensional ordered assembly of thin-shell Au/TiO_2 hollow nanospheres for enhanced visible-light-driven photocatalysis, *Angew. Chem. Int. Ed.* 53 (2014) 6618–6623.
- [8] Q. Liang, Z. Li, X. Yu, Z.H. Huang, F. Kang, Q.H. Yang, Macroscopic 3D porous graphitic carbon nitride monolith for enhanced photocatalytic hydrogen evolution, *Adv. Mater.* 27 (2015) 4634–4639.
- [9] Y. Fan, W. Ma, D. Han, S. Gan, X. Dong, L. Niu, Convenient recycling of 3D $\text{AgX}/\text{Graphene}$ aerogels ($\text{X} = \text{Br}, \text{Cl}$) for efficient photocatalytic degradation of water pollutants, *Adv. Mater.* 27 (2015) 3767–3772.
- [10] G. Cheng, H.M. Yang, K.F. Rong, Z. Lu, X.L. Yu, R. Chen, Shape-controlled solvothermal synthesis of bismuth subcarbonate nanomaterials, *J. Solid State Chem.* 183 (2010) 1878–1883.
- [11] Y. Zhang, D. Li, Y. Zhang, X. Zhou, S. Guo, L. Yang, Graphene-wrapped $\text{Bi}_2\text{O}_3\text{CO}_3$ core-shell structures with enhanced quantum efficiency profit from an ultrafast electron transfer process, *J. Mater. Chem. A* 2 (2014) 8273–8280.
- [12] X. Zhang, Y. Zheng, D.G. McCulloch, L.Y. Yeo, J.R. Friend, D.R. MacFarlane, Controlled morphogenesis and self-assembly of bismuthite nanocrystals into three-dimensional nanostructures and their applications, *J. Mater. Chem. A* 2 (2014) 2275–2282.
- [13] F. Dong, W.K. Ho, S.C. Lee, Z.B. Wu, M. Fu, S.C. Zou, Y. Huang, Template-free fabrication and growth mechanism of uniform $(\text{BiO})_2\text{CO}_3$ hierarchical hollow microspheres with outstanding photocatalytic activities under both UV and visible light irradiation, *J. Mater. Chem.* 21 (2011) 12428–12436.
- [14] T. Zhao, J. Zai, M. Xu, Q. Zou, Y. Su, K. Wang, X. Qian, Hierarchical $\text{Bi}_2\text{O}_3\text{CO}_3$ microspheres with improved visible-light-driven photocatalytic activity, *CrystEngComm* 13 (2011) 4010–4017.
- [15] F. Dong, S.C. Lee, Z. Wu, Y. Huang, M. Fu, W.K. Ho, S. Zou, B. Wang, Rose-like monodisperse bismuth subcarbonate hierarchical hollow microspheres: one-pot template-free fabrication and excellent visible light photocatalytic activity and photochemical stability for NO removal in indoor air, *J. Hazard. Mater.* 195 (2011) 346–354.
- [16] X.F. Cao, L. Zhang, X.T. Chen, Z.L. Xue, Persimmon-like $(\text{BiO})_2\text{CO}_3$ microstructures: hydrothermal preparation, photocatalytic properties and their conversion into Bi_2S_3 , *CrystEngComm* 13 (2011) 1939–1945.
- [17] F. Dong, T. Xiong, R. Wang, Y. Sun, Y. Jiang, Growth mechanism and photocatalytic activity of self-organized N-doped $(\text{BiO})_2\text{CO}_3$ hierarchical nanosheet microspheres from bismuth citrate and urea, *Dalton Trans.* 43 (2014) 6631–6642.
- [18] T. Xiong, H. Huang, Y. Sun, F. Dong, In situ synthesis of a C-doped $(\text{BiO})_2\text{CO}_3$ hierarchical self-assembly effectively promoting visible light photocatalysis, *J. Mater. Chem. A* 3 (2015) 6118–6127.
- [19] N. Liang, J. Zai, Miao Xu, Q. Zhu, X. Wei, X. Qian, Novel $\text{Bi}_2\text{S}_3/\text{Bi}_2\text{O}_3\text{CO}_3$ heterojunction photocatalysts with enhanced visible light responsive activity and wastewater treatment, *J. Mater. Chem. A* 2 (2014) 4208–4216.
- [20] F. Dong, Q. Li, Y. Sun, W.K. Ho, Noble metal-like behavior of plasmonic Bi particles as a cocatalyst deposited on $(\text{BiO})_2\text{CO}_3$ microspheres for efficient visible light photocatalysis, *ACS Catal.* 4 (2014) 4341–4350.
- [21] Q. Li, X. Hao, X. Guo, F. Dong, Y. Zhang, Controlled deposition of Au on $(\text{BiO})_2\text{CO}_3$ microspheres: the size and content of Au nanoparticles matter, *Dalton Trans.* 44 (2015) 8805–8811.
- [22] H. Wang, L. Zhang, Z. Chen, J. Hu, S. Li, Z. Wang, J. Liu, X. Wang, Semiconductor heterojunction photocatalysts: design, construction, and photocatalytic performances, *Chem. Soc. Rev.* 43 (2014) 5234–5244.
- [23] Y. Ma, X. Wang, Y. Jia, X. Chen, H. Han, C. Li, Titanium dioxide-based nanomaterials for photocatalytic fuel generations, *Chem. Rev.* 114 (2014) 9987–10043.
- [24] A. Di Paola, L. Palmisano, A.M. Venezia, V. Augugliaro, Coupled semiconductor systems for photocatalysis. preparation and characterization of polycrystalline mixed WO_3/WS_2 powders, *J. Phys. Chem. B* 103 (1999) 8236–8244.
- [25] S. Ida, A. Takashiba, S. Koga, H. Hagiwara, T. Ishihara, Potential gradient and photocatalytic activity of an ultrathin p–n junction surface prepared with two-dimensional semiconducting nanocrystals, *J. Am. Chem. Soc.* 136 (2014) 1872–1878.
- [26] M. Lu, C. Shao, K. Wang, N. Lu, X. Zhang, P. Zhang, M. Zhang, X. Li, Y. Liu, P-MoO₃ nanostructures/n-TiO₂ nanofiber heterojunctions: controlled fabrication and enhanced photocatalytic properties, *ACS Appl. Mater. Interfaces* 6 (2014) 9004–9012.
- [27] H. Wang, S. Li, L. Zhang, Z. Chen, J. Hu, R. Zou, K. Xu, G. Song, H. Zhao, J. Yang, Surface decoration of Bi_2WO_6 superstructures with Bi_2O_3 nanoparticles: an efficient method to improve visible-light-driven photocatalytic activity, *CrystEngComm* 15 (2013) 9011–9019.
- [28] P. Zhou, J. Yu, M. Jaroniec, All-solid-state Z-scheme photocatalytic systems, *Adv. Mater.* 26 (2014) 4920–4935.
- [29] D. Xu, B. Cheng, S. Cao, J. Yu, Enhanced photocatalytic activity and stability of Z-scheme Ag_2CrO_4 -GO composite photocatalysts for organic pollutant degradation, *Appl. Catal. B: Environ.* 164 (2015) 380–388.
- [30] J. Yu, S. Wang, J. Low, W. Xiao, Enhanced photocatalytic performance of direct Z-scheme g-C₃N₄-TiO₂ photocatalysts for the decomposition of formaldehyde in air, *Phys. Chem. Chem. Phys.* 15 (2013) 16883–16890.
- [31] W.K. Jo, J.Y. Lee, T.S. Natarajan, Fabrication of hierarchically structured novel redox-mediator-free ZnIn_2S_4 marigold flower/ Bi_2WO_6 flower-like direct

- Z-scheme nanocomposite photocatalysts with superior visible light photocatalytic efficiency, *Phys. Chem. Chem. Phys.* 18 (2016) 1000–1016.
- [32] P. Li, Y. Zhou, H. Li, Q. Xu, X. Meng, X. Wang, M. Xiao, Z. Zou, All-solid-state Z-scheme system arrays of $\text{Fe}_2\text{V}_4\text{O}_{13}/\text{RGO}/\text{CdS}$ for visible light-driving photocatalytic CO_2 reduction into renewable hydrocarbon fuel, *Chem. Commun.* 51 (2015) 800–803.
- [33] D. Zheng, C. Pang, X. Wang, The function-led design of Z-scheme photocatalytic systems based on hollow carbon nitride semiconductors, *Chem. Commun.* 51 (2015) 17467–17470.
- [34] H. Kato, Y. Sasaki, N. Shirakura, A. Kudo, Synthesis of highly active rhodium-doped SrTiO_3 powders in Z-scheme systems for visible-light-driven photocatalytic overall water splitting, *J. Mater. Chem. A* 1 (2013) 12327–12333.
- [35] J. Cao, X. Li, H. Lin, S. Chen, X. Fu, In situ preparation of novel p-n junction photocatalyst $\text{BiOI}/(\text{BiO})_2\text{CO}_3$ with enhanced visible light photocatalytic activity, *J. Hazard Mater.* 239–240 (2012) 316–324.
- [36] N. Liang, M. Wang, L. Jin, S. Huang, W. Chen, M. Xu, Q. He, J. Zai, N. Fang, X. Qian, Highly efficient $\text{Ag}_2\text{O}/\text{Bi}_2\text{O}_3\text{CO}_3$ p–n heterojunction photocatalysts with improved visible-light responsive activity, *ACS Appl. Mater. Interfaces* 6 (2014) 11698–11705.
- [37] Y. Zhu, Q. Ling, Y. Liu, H. Wang, Y. Zhu, Photocatalytic H_2 evolution on MoS_2 - TiO_2 catalysts synthesized via mechanochemistry, *Phys. Chem. Chem. Phys.* 17 (2015) 933–940.
- [38] Y.F. Zhao, Z.Y. Yang, Y.X. Zhang, L. Jing, X. Guo, Z. Ke, P. Hu, G. Wang, Y.M. Yan, K.N. Sun, Cu_2O decorated with cocatalyst MoS_2 for solar hydrogen production with enhanced efficiency under visible light, *J. Phys. Chem. C* 118 (2014) 14238–14245.
- [39] J. Liao, B. Sa, J. Zhou, R. Ahuja, Z. Sun, Design of high-efficiency visible-light photocatalysts for water splitting: $\text{MoS}_2/\text{AlN}(\text{GaN})$ heterostructures, *J. Phys. Chem. C* 118 (2014) 17594–17599.
- [40] M. Shen, Z. Yan, L. Yang, P. Du, J. Zhang, B. Xiang, MoS_2 nanosheet/ TiO_2 nanowire hybrid nanostructures for enhanced visible-light photocatalytic activities, *Chem. Commun.* 50 (2014) 15447–15449.
- [41] J. Zhang, Z. Zhu, X. Feng, Construction of two-dimensional MoS_2/CdS p–n nanohybrids for highly efficient photocatalytic hydrogen evolution, *Chem. Eur. J.* 20 (2014) 10632–10635.
- [42] C. Liu, L. Wang, Y. Tang, S. Luo, Y. Liu, S. Zhang, Y. Zeng, Y. Xu, Vertical single or few-layer MoS_2 nanosheets rooting into TiO_2 nanofibers for highly efficient photocatalytic hydrogen evolution, *Appl. Catal. B: Environ.* 164 (2015) 1–9.
- [43] Q. Wang, G. Yun, Y. Bai, N. An, J. Lian, H. Huang, B. Su, Photodegradation of rhodamine B with $\text{MoS}_2/\text{Bi}_2\text{O}_3\text{CO}_3$ composites under UV light irradiation, *Appl. Surf. Sci.* 313 (2014) 537–544.
- [44] C. Zhao, J. Kong, X. Yao, X. Tang, Y. Dong, S.L. Phua, X. Lu, Thin MoS_2 nanoflakes encapsulated in carbon nanofibers as high-performance anodes for lithium-ion batteries, *ACS Appl. Mater. Interfaces* 6 (2014) 6392–6398.
- [45] T. Xiong, F. Dong, Z. Wu, Enhanced extrinsic absorption promotes the visible light photocatalytic activity of wide band-gap $(\text{BiO})_2\text{CO}_3$ hierarchical structure, *RSC Adv.* 4 (2014) 56307–56312.
- [46] Y. Hou, A.B. Laursen, J. Zhang, G. Zhang, Y. Zhu, X. Wang, S. Dahl, I. Chorkendorff, Layered nanojunctions for hydrogen-evolution catalysis, *Angew. Chem. Int. Ed.* 52 (2013) 3621–3625.
- [47] K.S.W. Sing, D.H. Everett, R.A.W. Haul, L. Moscou, R.A. Pierotti, J. Rouquerol, T. Siemieniewska, Reporting physisorption data for gas/solid systems with special reference to the determination of surface area and porosity, *Pure Appl. Chem.* 57 (1985) 603–619.
- [48] Z. Hosseini, N. Taghavinia, N. Sharifi, M. Chavoshi, M. Rahman, Fabrication of high conductivity TiO_2/Ag fibrous electrode by the electrophoretic deposition method, *J. Phys. Chem. C* 112 (2008) 18686–18689.
- [49] M.R. Hoffmann, S.T. Martin, W. Choi, D.W. Bahnemann, Environmental applications of semiconductor photocatalysis, *Chem. Rev.* 95 (1995) 69–96.
- [50] M. Ou, F. Dong, W. Zhang, Z. Wu, Efficient visible light photocatalytic oxidation of NO in air with band-gap tailored $(\text{BiO})_2\text{CO}_3$ – BiOI solid solutions, *Chem. Eng. J.* 255 (2014) 650–658.
- [51] H. Li, K. Yu, X. Lei, B. Guo, H. Fu, Z. Zhu, New insights into BiVO_4 properties as visible light photocatalyst, *J. Phys. Chem. C* 119 (2015) 22681–22689.